Ultralong Silver Trimolybdate Nanowires: Synthesis, Phase Transformation, Stability, and Their Photocatalytic, Optical, and Electrical Properties

Mei Feng, Meng Zhang, Ji-Ming Song, Xiao-Guang Li, and Shu-Hong Yu*

Division of Nanomaterials & Chemistry, Hefei National Laboratory for Physical Sciences at Microscale, Department of Chemistry, National Synchrotron Radiation Laboratory, University of Science and Technology of China, Hefei 230026, People's Republic of China

ABSTRACT Ultralong orthorhombic silver trimolybdate nanowires (NWs) can be synthesized by a simple hydrothermal process without using any structure directing agent. Their phase transformation and stability to thermal and modeling sunlight from a Xe lamp have been systematically studied. Well-dispersed Ag nanoparticles can *in situ* form on the backbone of the nanowires by photoirradiation, and their photocatalytic and optical properties have been investigated. The investigations on photocatalytic, photoluminescent, and surface-enhanced Raman scattering (SERS) of the as-synthesized nanowires indicate that these nanowires loaded with Ag nanoparticles by photoirradiation can be a new kind of photocatalytic and luminescent material and potentially can be used as an efficient SERS substrate. The electrical conductivity of an individual nanowire exhibits almost nonlinear and symmetric current/voltage (*I*/*V*) characteristics for bias voltages in the range of −5 to 5 V. Ohmic mechanism, Schottky, and the Poole-Frenkel emission play an important part, respectively, in low, medium, and high electrical fields.

KEYWORDS: silver trimolybdates · photoirradiation · photocatalytic · photoluminescence · electrical conductivity · surface-enhanced Raman scattering (SERS)

Metal molybdates, as an important family of inorganic materials, have been an intense focus because of their strong potential application in various fields such as photoluminescence,[1,2] microwave applications,[3] optical fibers,[4] scintillator materials,[5] humidity sensors,[6] magnetic properties,[7] and catalysts.[8] Especially, low-dimensional (1D) metal molybdates/tungstates[9−11] have attracted much interest in recent years.

Silver molybdates, as one kind of metal molybdates, such as $Ag_6Mo_{10}O_{33}$, $Ag_2Mo_2O_7$, and $Ag_2Mo_4O_{13}$ nanowires (NWs),[9] wire-like Ag_2MoO_4,[12] and $Ag_2Mo_3O_{10}\cdot 1.8H_2O$,[13] have attracted much attention, due to their important application in conducting glass[14−18] and ammonia sensing material.[18,19] During the past decades, methods of preparing silver molybdates have been proposed, but most of them are traditionally synthesized by straight and harsh reaction in the MoO_3/Ag_2O system.[20,21] Recently, solution synthesis of low-dimensional silver molybdate nanostructures has been reported.[9,12,22] For example, Cui *et al.* have prepared ultralong $Ag_6Mo_{10}O_{33}$ NWs.[9] Nagaraju *et al.* reported the synthesis of silver molybdate nanorods/nanowires/multipods.[22] Cheng *et al.* have synthesized uniform one-dimensional Ag_2MO_4 (M = Cr, Mo, and W).[12] All of these advances in synthesis make it possible to further investigate the novel properties of silver molybdates. Up to now, several works have been done to explore their potential properties and practical applications.[12,22] For example, Cheng *et al.* studied photoswitches of one-dimensional Ag_2MO_4 (M = Cr, Mo, and W).[12] Nagaraju *et al.* reported the photoluminescence property of silver molybdate multipods.[22] However, to the best of our knowledge, solution synthesis and the thermal stability of silver trimolybdate NWs, electrical conductivity property of a single-crystalline nanowire, especially the potential applications in optical and electrics, have not been investigated yet.

On the other hand, visible-light-driven plasmonic photocatalysts have gained much attention currently, and they have been considered as one of the most promising alternatives.[23] Besides, silver nanoparticles (NPs) have an efficient plasmon resonance in the visible region and would enhance the activity of plasmonic photocatalysts.[23−27] A great number of composite semiconductor photocatalysts, including Ag/TiO_2,[24,26,28−30] SnO_2/TiO_2,[31,32] $H_2WO_4\cdot H_2O$/AgCl,[33] ZnO/In_2O_3,[34] Bi_2O_3/BiOCl,[35] AgI/BiOI,[36] Ag/AgX (X = Br, Cl),[23,25,27] and so on, have proven effective photocatalytic properties. Interestingly, in our work, we

* Address correspondence to shyu@ustc.edu.cn.

Received for review June 21, 2011 and accepted July 19, 2011.

Published online July 19, 2011
10.1021/nn202296h

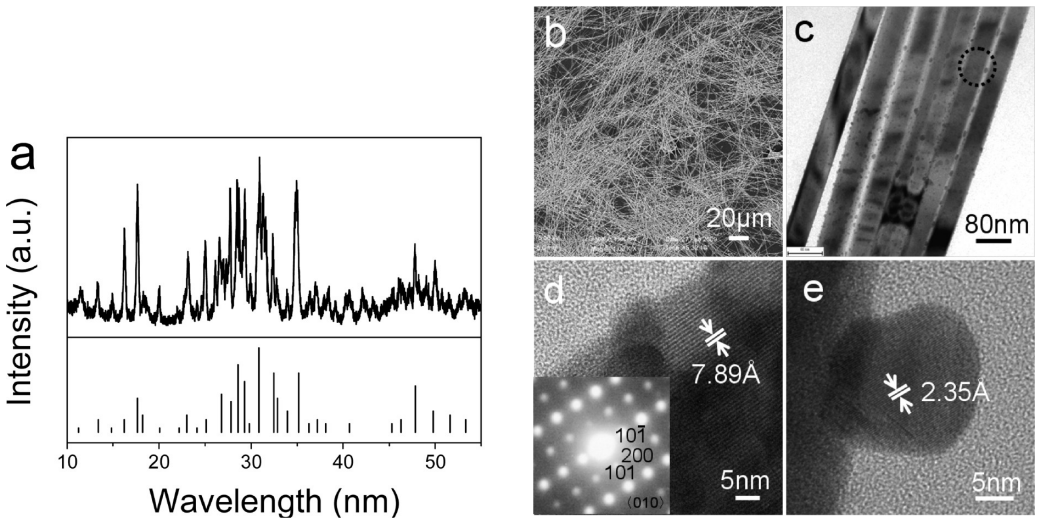

Figure 1. (a) XRD pattern of the silver trimolybdate NWs prepared at pH 2, 140 °C, 12 h with [$(NH_4)_6Mo_7O_{24}\cdot 4H_2O$] = 0.028 M and [$AgNO_3$] = 0.1 M. (b,c) FESEM and TEM images of the as-prepared silver trimolybdate NWs. Small nanoparticles appeared on the backbone of NWs during TEM observation. (d,e) Lattice-resolved HRTEM images and SAED patterns of a single nanowire and a typical nanoparticle were taken from the marked circular area in panel c.

figured out that the silver trimolybdate NWs can display excellent plasmonic photocatalytic performance under visible-light irradiation; in particular, the photo-irradiated NWs will exhibit better.

Herein, we report hydrothermal synthesis of ultralong orthorhombic silver trimolybdate NWs, phase transformation and stability to temperature and modeling sunlight from a Xe lamp, and the electrical property of an individual nanowire. In addition, the well-dispersed Ag nanoparticles can *in situ* form on the backbone of the nanowires, and their optical properties and photocatalytic property have been investigated.

RESULTS AND DISCUSSION

Structure and Morphology. The phase of the as-prepared silver trimolybdate NWs was examined by X-ray diffraction at room temperature (25 °C) in Figure 1a, and all of the diffraction peaks can be indexed as $Ag_2Mo_3O_{10}\cdot 1.8H_2O$ phase with orthorhombic crystal structure (JCPDS File No. 39-0045) with lattice parameters a = 13.20 and c = 9.76 Å. The as-prepared NWs show good stability in ambient environment. The scanning electron microscope (SEM) and transmission electron microscope (TEM) images in Figure 1b,c show uniform and ultralong silver trimolybdate NWs with lengths of at least several hundred micrometers and diameters of 80−200 nm. HRTEM image and selected area electron diffraction (SAED) patterns taken from the marked area of an individual nanowire in Figure 1b indicated that the lattice spacing of 7.89 Å was in good agreement with that of the lattice spacing of the (101) planes. The corresponding SAED pattern was taken along the [010] direction on the nanowires. The combination of HRTEM and SAED patterns indicated that high-quality single-crystalline silver trimolybdate NWs can be synthesized by the hydrothermal method.

When the NWs were exposed to electron beam, small nanoparticles (NPs) rapidly came into being on the surface of NWs due to the bombardment of high-energy electrons during the TEM observation, as shown in Figure 1c. A typical particle with a diameter of about 10−20 nm was characterized by the HRTEM image in Figure 1e. The lattice spacing of 2.35 Å is in agreement with the value of the lattice spacing of (111) plane of cubic Ag phase. Elemental dispersive spectra (EDS) were also taken from the marked circular area (Supporting Information Figure S1), showing the corresponding elements of the nanowires and the nanoparticles. The NWs with Ag NPs reduced *in situ* will have potential applications for catalytic applications and SERS detection, which we will discuss later.

Phase Transformation. Phase transformation of the as-prepared silver trimolybdate NWs was investigated by the XRD patterns, TG-DTA, and DSC analysis. Figure 2a shows the related XRD patterns at selected temperatures, and the detailed XRD analysis of phase compositions was investigated (Supporting Information Figure S2). TG-DTA analysis in Figure 2b shows that the NWs will undergo a distinct weight loss of 9.91 wt %. Here, the mass losses should be due to the loss of water, decomposition of the NWs and the escape of O_2, and a little sublimation of MoO_3. Figure 2c displayed the related DSC analysis at selected temperatures.

The mass loss before 250 °C in Figure 2b and the first endothermic effect in Figure 2c should correspond to the loss of water. However, considering the apparatus error, the decrease in mass was a little smaller than expected. The following mass loss and endothermic peaks before 500 °C should be due to the decompositions in the course of heating the samples. At about 300 °C, the large decrease in mass and the distinct endothermic peak could be due to decomposition and

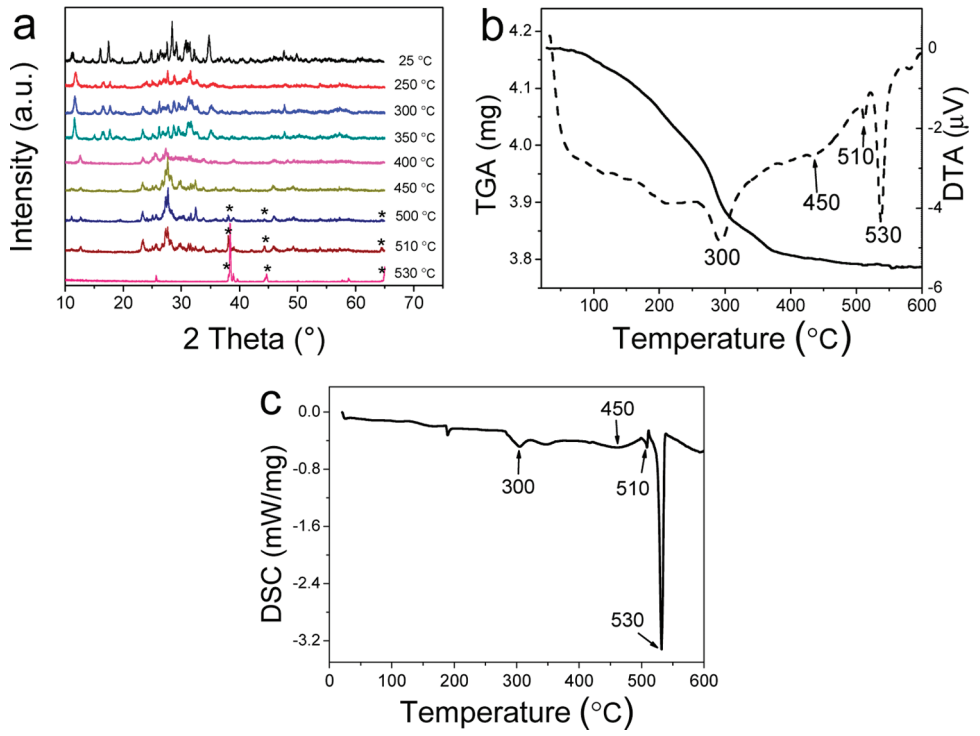

Figure 2. (a) XRD patterns of the as-prepared NWs after treatment at selected temperatures. At 25 °C, the XRD pattern was defined as orthorhombic $Ag_2Mo_3O_{10}\cdot 1.8H_2O$. Different phases were detected after treatment of the sample at selected temperatures. At about 530 °C, the final products were melted down. Note: the diffraction peak marked with ∗ can be indexed as cubic Ag phase. (b) TG-DTA and (c) DSC analysis of the as-prepared NWs exhibited a distinct weight loss of 9.91 wt % and several endothermic peaks from about 25 to 530 °C.

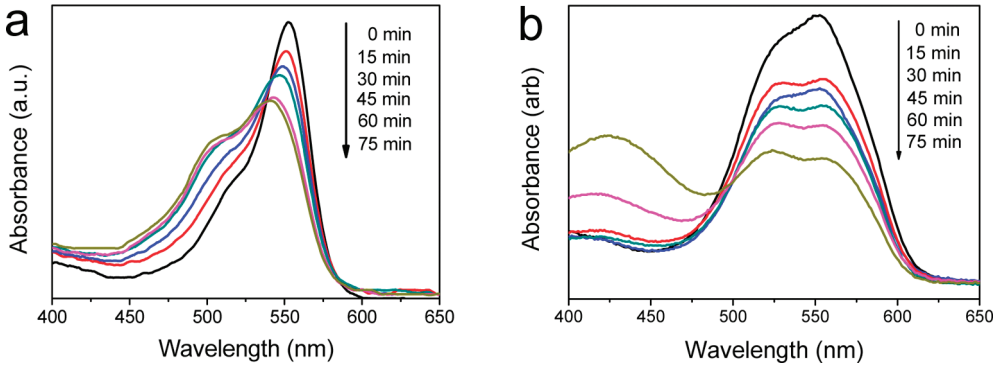

Figure 3. Time-dependent absorption spectra of the RhB solution (0.15 mM, 200 mL) which were obtained per 15 min. A certain amount of nanowires was added in the solution: (a) 20 mg of original NWs; (b) 20 mg of NWs after irradiation for 60 min under modeling sunlight from a 300 W Xe lamp.

escape of O_2. From the related XRD pattern (Supporting Information Figure S2b), molybdenum oxides and cubic Ag_2MoO_4 came into being according to the equation:

$$Ag_2Mo_3O_{10} \rightarrow Ag_2MoO_4 + 2MoO_2 + O_2\uparrow \quad (1)$$

According to the XRD pattern (Supporting Information Figure S2c), the subsequent decrease in mass and the faint endothermic peak at about 350 °C also corresponded to eq 1; however, the deceleration of decrease in mass should be connected with the little absorption of oxygen as shown in the following reaction:

$$2MoO_2 + O_2 \rightarrow 2MoO_3 \quad (2)$$

However, the amount of MoO_3 might be not enough to be detected. When the temperature was increased to about 400 °C, MoO_3 and Ag_2O were obtained according to the result of XRD analysis (Supporting Information Figure S2d):

$$Ag_2Mo_3O_{10} \rightarrow 3MoO_3 + Ag_2O \quad (3)$$

$$Ag_2MoO_4 \rightarrow MoO_3 + Ag_2O \quad (4)$$

The deceleration of decrease in mass should also be related to the absorption of oxygen (eq 2). As the temperature increases to 450 °C, it is interesting to observe that small amounts of disilver 13-oxotramolybdate ($Ag_2Mo_4O_{13}$) were detected (Supporting Information Figure S2e). The faint endothermic peak in Figure 3c should be due to the formation of

$Ag_2Mo_4O_{13}$:

$$4MoO_3 + Ag_2O \rightarrow Ag_2Mo_4O_{13} \quad (5)$$

In Figure 2a, small amounts of cubic Ag are detected at 500 °C, which meant that Ag_2O partly reacted with MoO_3 before the decomposition of silver oxide:[20]

$$Ag_2O \rightarrow 2Ag + 1/2O_2\uparrow \quad (6)$$

Plenty of Ag_2O and $Ag_2Mo_4O_{13}$ were decomposed with the temperature increase; as a result, large amounts of MoO_3 and Ag were detected at 510 °C (Supporting Information Figure S2g). Interestingly, during the process from 400 to 530 °C, MoO_3 was always present, which was not consumed completely (Supporting Information Figure S2e−2g).[20]

The endothermic effect at 530 °C in Figure 2c should correspond to the melting of MoO_3 and Ag.[20] It has been reported that the melting point of Ag NPs would be much lower than that of the bulk silver (960 °C) with the size decrease of NPs and the low-temperature metallization of the nanoparticles due to the decomposition of silver molybdates into silver metal and gas rather than the actual melting of silver metal.[37−40] From the XRD patterns at 530 °C (Figure 2a and Figure S2h), only small amounts of MoO_3 and cubic Ag phases are detected.

Photocatalysis. To demonstrate the potential application of these novel silver trimolybdate NWs in the degradation of organic contaminants, we have first investigated their photocatalytic activities by choosing the photocatalytic bleaching of RhB as a model reaction. As RhB could be degraded under irradiation of a Xe lamp without any photocatalysts, we have obtained time-dependent absorption spectra of RhB degradation with and without photocatalysts. Figure 3a showed the temporal evolution of the spectra during the photocatalytic bleaching of RhB solutions in the presence of the as-prepared NWs under visible illumination. Compared to the spectra of RhB degradation without any photocatalyst (Supporting Information Figure S3), it exhibited obvious diminishment of RhB, which indicated the photocatalytic activity of the as-prepared NWs. Nanomaterials deposited with silver NPs are expected to be catalytically active;[41−43] therefore, we used the photoirradiated NWs after light irradiation for 60 min as a photocatalysts for the same procedure (Figure 3b). The absorption intensities at about 430 nm were getting stronger and stronger. They should correspond to the absorption bands of Ag NPs due to photochemical decomposition or photocatalytic reduction of the photoirradiated NWs.[27,28] The spectra in Figure 3b showed photocatalytic activity higher than that of the as-prepared NWs, which should be due to the appearance of Ag NPs with high photocatalytic activity,[42] as silver NPs showed efficient plasmon resonance in the visible region, and the enhanced photocatalytic activities should be due to an effcient charge separation/transfer which are favored by the existence of Ag NPs.[23,27]

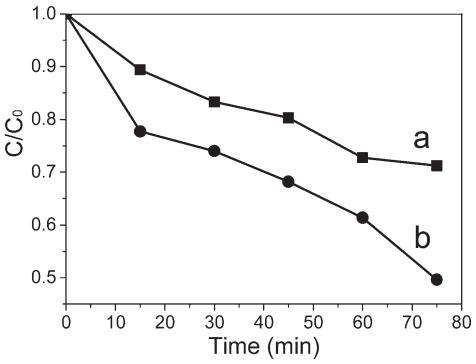

Figure 4. Photocatalytic bleaching of RhB (0.15 mM, 100 mL) using different samples: (a) 20 mg of original NWs; (b) 20 mg of NWs after irradiation for 60 min under modeling sunlight from a 300 W Xe lamp.

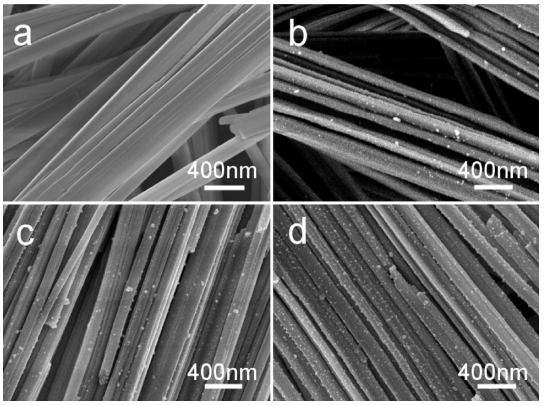

Figure 5. FE-SEM images of ultralong NWs after irradiation for 0, 10, 30, and 60 min under modeling sunlight from a Xe lamp in atmosphere. (a) Smooth surfaces were observed for the sample without irradiation. (b) A few NPs appeared on the backbones of NWs after being irradiated for 10 min. (c) More NPs were embedded on the NWs after irradiation for 30 min. (d) Many NPs were thickly and homogeneously dotted on the surfaces of NWs after irradiation for 60 min.

Compared to the absorption spectra of RhB degradation with and without photocatalysts, the efficiency was enhanced when the photocatalysts were added. We observed not only decreasing absorption bands but also the blue-shifted absorption peaks. It was reported that two processes have occurred: the photocatalytic process and the photosensitized process.[44−46] In the photocatalytic process, conjugate structures were degraded as confirmed by the decrease of the absorption band without shifting the maximum absorbance wavelength, while in the photosensitized process, ethyl groups of RhB were removed one-by-one as confirmed by the gradual blue-shifted absorption peaks.[44−46] It could be concluded that the blue-shifted shoulders should correspond to the degradation of tetraethylated RhB into monoethylated (510 nm) and diethylated (522 nm) RhB.[47] We believed that, if the irradiation time increased, the N-de-ethylation of RhB would be fully degraded.

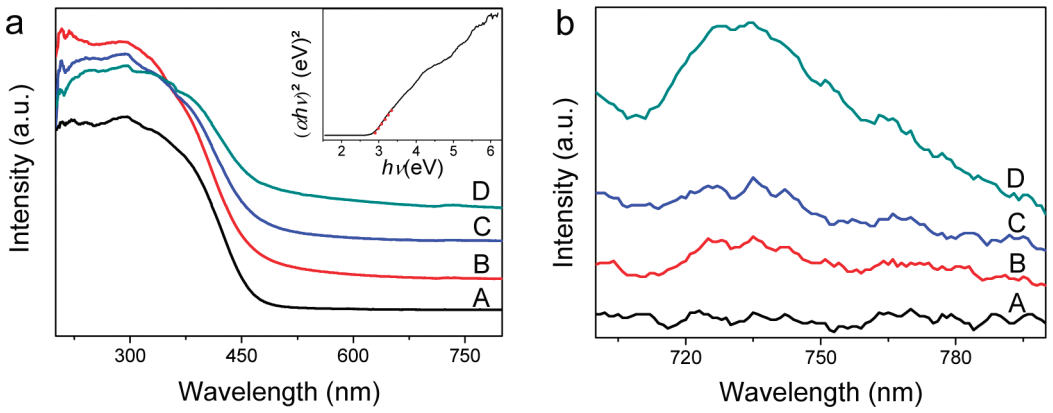

Figure 6. (a) UV−visible absorption spectra of silver trimolybdate NWs with irradiation times of (A) 0, (B) 10, (C) 30, and (D) 60 min. Weak peaks appeared in the spectral region between 700 and 800 nm. Inset in the top right corner showed the plots of $(\alpha h\nu)^2$ *versus* energy ($h\nu$) for the band gap energy of the as-prepared NWs. (b) Magnified spectra in the spectral region between 700 and 800 nm corresponding to panel a. As the irradiation time increased, the intensities of absorbance around 730 nm became stronger and stronger.

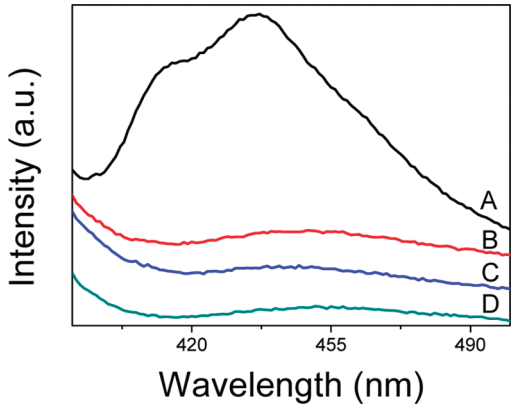

Figure 7. Photoluminescence (PL) spectra of the as-prepared original silver trimolybdate NWs and photoirradiated NWs at room temperature. (A) Two weak violet emissions were observed at 415 and 437 nm, and a very weak blue emission was at 463 nm. (B−D) After being irradiated for 10, 30, and 60 min, intensities of these peaks became obviously weakened.

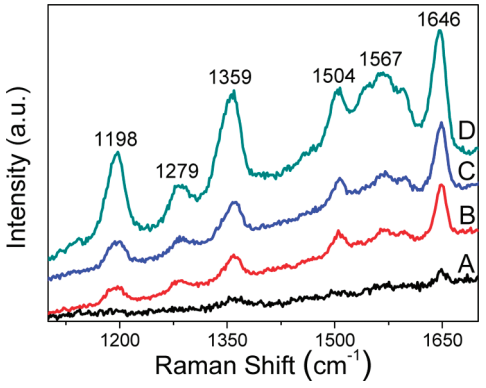

Figure 8. Surface-enhanced Raman scattering spectra of the prepared samples after irradiation for different time intervals: (A) 0 min, (B) 10 min, (C) 30 min, and (D) 60 min.

The photocatalytic bleaching curves of RhB using these two samples as photocatalysts are shown in Figure 4. It can be easily figured out that the photocatalytic bleaching of RhB using the NWs after photoirradiation for 60 min as catalysts is 25% higher than that using the as-prepared NWs. It is suggested that these silver trimolybdate NWs would have photocatalytic activity and could be used as photocatalyst.

UV−Vis and Photoluminescence. FESEM images in Figure 5 show the photoirradiated NWs under modeling sunlight for 0, 10, 30, and 60 min at ambient temperature. Obviously, Ag NPs formed on the surface of NWs after photoirradiation. Figure 5a shows smooth surfaces of NWs without irradiation. After irradiation for 10 min, a few nanoparticles appeared on the backbones of NWs (Figure 5b). Whe the irradiation time was prolonged to 30 min, the particles became denser and denser (Figure 5c). After they were irradiated for 60 min, many nanoparticles formed densely and were distributed homogeneously on the surfaces of NWs (Figure 6d).

UV−visible absorption spectroscopy is a useful technique to monitor the size-dependent optical properties of nanomaterials, due to the quantum confinements of the photogenerated electron−hole carriers in the particles.[22] Figure 6a shows the UV−visible absorption spectra of silver trimolybdate NWs with different irradiation time. It can be figured out that the NWs absorbed in the spectral region between 200 and 600 nm and had a maximum absorbance around 302 nm. From the plots of $(\alpha h\nu)^2$ *versus* energy ($h\nu$) in the inset, the band gap energy of the as-prepared NWs was determined to be about 2.8 eV. The plasmonic absorption bands of Ag NPs at about 410 nm become intense; however, they were not distinct enough, as the optical absorption of silver trimolybdate overlapped the plasmonic absorption bands of Ag NPs. Interestingly, we noticed that weak peaks appeared in the spectral region between 700 and 800 nm, and the intensities of the peaks get stronger and stronger with increasing irradiation time. Details are shown in Figure 6b, which

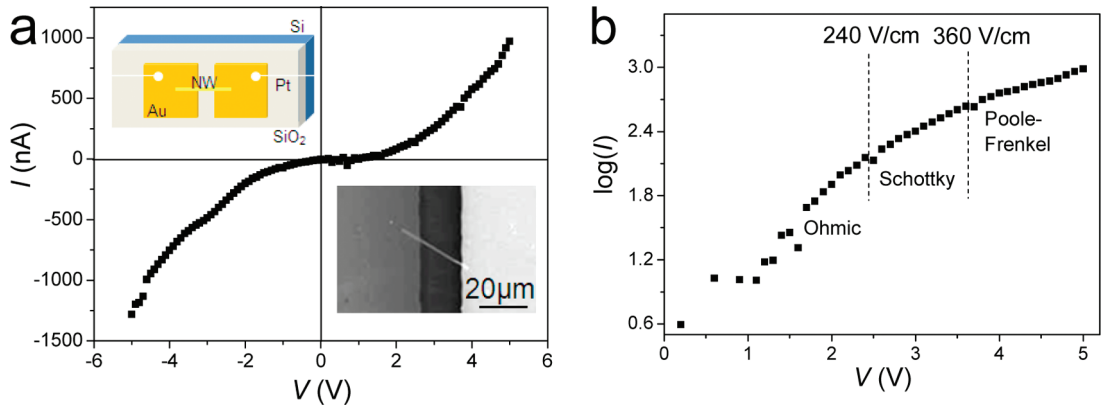

Figure 9. (a) Current−voltage (*I*−*V*) curve of the gold electrode with an individual nanowire. Inset in the top left corner shows a schematic view, and the bottom right one shows the SEM image of connection. (b) Positive part of the *I*−*V* curve on the scale of log(*I*). Three fields have been exhibited.

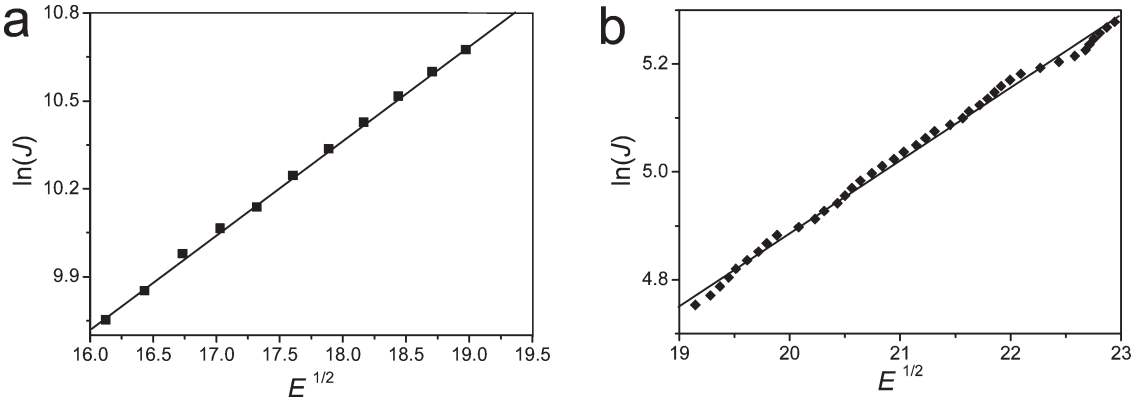

Figure 10. Plot of ln(*J*) *vs* $E^{1/2}$ from Figure 9b. (a) Electric field between 240 and 360 V/cm; (b) electric field more than 360 V/cm.

are the magnified spectra in the spectral region between 700 and 800 nm shown in Figure 6a. The results indicated that the intensity increased as more Ag NPs aggregate together on the NWs with prolonged irradiation time. It is clear evidence of the aggregation of isolated Ag^+ ions into Ag^0 clusters.[48−50]

Room temperature photoluminescence (PL) spectra of the as-synthesized NWs are shown in Figure 7, obtained with an excitation wavelength of 360 nm. Figure 7A exhibited two violet emissions at 437 and 415 nm and a very weak blue emission at 463 nm. The blue band emission could be due to the charge transfer transition within the $[MoO_4]^{2-}$ complex.[51,52] The violet emissions were attributed to the exciton transition.[53] Lines B−D of Figure 7 show PL spectra of the NWs after being irradiated for 10, 30, and 60 min, respectively. Luminescence intensity is weakened distinctly in these spectra compared with that in Figure 7A, and the blue band emission disappeared with prolonged irradiation time. It could be explained that longer light irradiation would result in the formation of more silver NPs with tens of nanometers on the backbone of NWs, and the silver NPs are responsible for the fluorescence decay.[54] It is suggested that the dotted silver on the backbone of NWs may add the surface nonradiative recombination sites, which would depress the photoluminescence quantum yields.[55,56]

SERS. To demonstrate the potential application of the as-synthesized ultralong silver trimolybdate NWs in SERS for molecular sensing with high sensitivity and specificity, we have used them as SERS substrates to investigate the surface-enhanced Raman excitation spectroscopy of Rhodamine 6G (R6G) molecules.

Room temperature Raman spectrum of the as-prepared NWs has been obtained before the SERS experiments, and all of the peaks have been defined to illuminate the composition of the as-prepared NWs (Supporting Information Figure S4). In sequence, a series of irradiation time-dependent SERS of R6G molecules absorbed on the NWs films have been set up in Figure 8. The spectra were collected with irradiation times of 0, 10, 30, and 60 min. It is clearly shown that Raman signal intensities of R6G on the NWs with Ag decoration were increasing intensively. Figure 8 implies that the more the silver NPs embedded on the films, the stronger the intensities for most bands. Therefore, it can be determined that the samples after light inducement had better performance on SERS effect, and light inducement is an effective way to modify the performances of the nanowires.

The defined spectrum of the silver trimolybdate NWs after irradiation for 60 min is shown in Figure 8D. The peaks located at 1646, 1567, 1504, 1359, 1279, and 1198 cm^{-1} are in agreement with those for R6G.[57] The characteristic vibration modes of R6G molecules were observed, and they were assigned as ν154, ν150, ν146, ν118, ν111, and ν105.[57] The observed Raman bands can be assigned as ν(C−C) stretching mode at 1646, 1567, 1504, and 1359 cm^{-1} and ν(C−O−C) stretching mode at 1279 cm^{-1}.[58] However, as the number of R6G molecules absorbed on the NWs after photoirradiation could not be determined with the method described in the Materials and Methods, the surface enhancement factor (EF) was not evaluated. It should be noted that the detailed work on calculating EF of the photoinduced NWs needs more attention in the future. The results demonstrated that this kind of NW would potentially be a SERS substrate candidate.

Electrical Properties. The electrical property for the silver trimolybdate NWs has not been reported previously. To the best of our knowledge, a lot of research work has been focused on the electrical properties of silver ion conducting glasses,[15−17] AgI-doped silver molybdates glasses,[59−61] and β-$AgVO_3$.[62,63] Herein, we discuss the electrical conductivity property of an individual single-crystal silver trimolybdate NW by scanning the bias voltage at room temperature and under ambient conditions. Due to the existence of Ag^+ cations between the molybdate layers in the structure,[18] the as-synthesized NWs were expected to have a good electrical conductivity for potential applications in microelectrodes or nanodevices.[62,63]

To investigate the electrical conductivity properties, we measured the current−voltage (*I*−*V*) curve of an individual nanowire. Insets in Figure 9a show the contact and measurement with the effective length and cross section of the sample, which are approximately 10^{-2} cm and 100×50 nm^2, respectively. The *I*−*V* curve of an individual nanowire at room temperature is shown in Figure 9a. It is obvious that the bottom-contacted device exhibited nonlinear and almost symmetric current−voltage (*I*−*V*) characteristics for bias voltages in the range of −5 to 5 V, and the obtained characteristic was almost symmetrical and behaved almost linearly for an electrical field lower than 240 V/cm. This behavior may be explained by the ohmic mechanism of conductivity in the low electrical field (less than 240 V/cm). The measurement was reproducible, and no large fluctuations were observed even in the high bias region, indicating that the device was stable.

Because the thickness of the nanowire is more than 50 nm, the tunnel current can be ignored. A further increase in the applied voltages resulted in an exponential behavior. To study the electrical conduction mechanism of the NWs in a higher field, we have established the positive part of the *I*−*V* curve in Figure 9b. The logarithm of the current density [ln(*J*)] was also plotted against the square root of the electric field [$E^{1/2}$] in Figure 10. It can be determined that the straight-line nature observed at a medium electric field between 240 and 360 V/cm implied the Schottky mechanism,[64,65] as shown in Figure 10a, while at high electrical fields, the observed straight line in Figure 10b was related to the Poole-Frenkel mechanism.[64,66] It is anticipated that the novel silver trimolybdate single-crystalline NWs may have unique applications in microelectrodes or microsensors, which is similar to the novel vanadate materials.[64−66]

CONCLUSION

In summary, ultralong and uniform silver trimolybdate NWs have been synthesized by a facile hydrothermal process without any structure directing agents. Phase transition of the as-prepared silver trimolybdate NWs at selected temperatures revealed their stability to thermal and photoirradiation experiments, showing their light stability, which also provided clear evidence for the aggregation of isolated Ag^+ ions into Ag^0 clusters. What is more, photocatalytic, optical, and SERS results demonstrated that photoirradiation would provide an effective way to modify the chemical/physical performances of the NWs and indicated the potential applications in photocatalysts, photoluminescence, and SERS substrates for the photoirradiated silver trimolybdate NWs. The current−voltage (*I*/*V*) curves of an individual nanowire exhibited the electrical conduction mechanisms of the nanowire. Ohmic mechanism played an important role at low electrical fields; Schottky emission worked at medium electrical fields; while the Poole-Frenkel emission in this case should be the preferable mechanism at high electrical fields. This kind of silver trimolybdate NW is expected to have practical applications in photocatalysis, microelectrodes, or sensors.

MATERIALS AND METHODS

All reagents are of analytical grade and used without further purification.

Materials and Preparation. Analytical grade $AgNO_3$ and $(NH_4)_6Mo_7O_{24}$ were purchased from Shanghai Chemical Industrial Company. The reaction was carried out in a 30 mL capacity Teflon-lined stainless steel autoclave, which was done in a digital-type temperature-controlled oven.

The preparation of ultralong silver trimolybdate NWs was based on the procedure reported previously with slight modification. In this synthesis, the reaction was carried out at pH 2, in a 30 mL capacity Teflon-lined stainless steel autoclave. Then, 877.5 mg (0.71 mmol) of analytical grade $(NH_4)_6Mo_7O_{24}\cdot 4H_2O$ and 424.7 mg (2.5 mmol) $AgNO_3$ were dissolved in 15 and 10 mL of distilled water, respectively. The precursor solution was transferred into a Teflon-lined

stainless autoclave and maintained at 140 °C for 12 h. Then, final products were washed and dried in a vacuum at 50 °C for 8−12 h.

Phase Transformation. Differential thermal analysis/thermogravimetry (DTA/TG) and differential scanning calorimetry (DSC) thermal analyses were performed on a TGA-50 thermal analyzer (Shimadzu Corporation) with a heating rate of 10 °C min^{-1} in flowing nitrogen. X-ray diffraction (XRD) patterns for all of the samples were recorded on a MAC Science Co. Ltd. MXP 8 AHF X-ray diffractometer with monochromatized Cu Kα radiation (λ = 1.54056 Å) at selected temperatures.

Light Inducement, PL, and Photocatalysis. To investigate the light-induced property, the solution of NWs was deposited on sheet copper (1 × 1 cm^2) to engender films and then irradiated for 0, 10, 30, and 60 min under modeling sunlight to induce the formation of Ag NPs from the as-prepared nanowires. PL spectra were performed on a Fluorolog3-TAU-P at room temperature with an excitation wavelength of 360 nm.

The photocatalytic activities of the as-prepared and photoirradiated NWs were first evaluated by degradation of Rhodamine B (RhB) solution under modeling sunlight from a 300 W Xe lamp. Twenty milligrams of as-prepared and photoirradiated NWs were poured into 200 mL RhB aqueous solution (0.15 mM) in a Pyrex reactor at room temperature. Before light was turned on, both solutions were stirred for 30 min in the dark to ensure the establishment of an adsorption−desorption equilibrium. The concentrations of RhB during the degradation were monitored by colorimetry using a UV−vis spectrometer.

Surface-Enhanced Raman Scattering (SERS). R6G was used as probe molecules to evaluate the SERS activities of Ag NPs dotted on the backbones of the NWs. Fifteen microliters of R6G ethanol aqueous solution with 0.15 mM was dropped slowly onto the films deposited on sheet copper mentioned above to catch hold of surface molecules. The specimens were laid in the air at ambient temperature to vaporize the residual droplets of the surface naturally. Surface-enhanced Raman spectra were acquired by a Ranishaw Raman microscope operated with a 514.5 nm argon laser (beam size ~2 μm).

Electrical Conductivity Measurement. Electrical conductivity of an individual nanowire was carried out on the Agilent E5270 *I*−*V* parametric measurement system. To make electrical contact with an individual nanowire, a diluted aqueous suspension of NWs was stochastically dropped and dried on an oxidized silicon substrate, on which contacts of gold had been evaporated through a shadow mask in an early operation (photoetching method). The spacing intervals among gold contacts are 10 μm. Two platinum wire electrodes were derived from the two gold contact dots with silver paste.

Characterization. The products were characterized by X-ray diffraction pattern (XRD) and recorded on a MAC Science Co. Ltd. MXP 8 AHF X-ray diffractometer with monochromatized Cu Kα radiation (λ = 1.54056 Å). The morphology and structure were examined with a JEOL JSM-6700F scanning electron microscope (SEM), a transmission electron microscope (TEM) performed on a Hitachi (Tokyo, Japan) H-800 transmission electron microscope (TEM) at an accelerating voltage of 200 kV, selected area electron diffraction (SAED), and a high-resolution transmission electron microscope (HRTEM) (JEOL-2010) operated at an acceleration voltage of 200 kV. Energy-dispersive X-ray (EDX) analysis was obtained with an EDAX detector installed on the same HRTEM. UV−vis spectra were recorded on UV-2501PC/2550 at room temperature (Shimadzu Corporation, Japan).

Acknowledgment. S.-H.Y. acknowledges the special funding support from the National Basic Research Program of China (2010CB934700), the National Natural Science Foundation of China (NSFC, Nos. 91022032, 50732006), and the International Science & Technology Cooperation Program of China (2010DFA41170), and the Principle Investigator Award by the National Synchrotron Radiation Laboratory at the University of Science and Technology of China.

Supporting Information Available: EDS, photos and XRD analysis at selected temperatures, time-dependent absorption spectra of the RhB solution without any photocatalysts. Room temperature Raman spectrum. This material is available free of charge *via* the Internet at http://pubs.acs.org.

REFERENCES AND NOTES

1. Qi, T.; Takagi, K.; Fukazawa, T. Scintillation Study of $ZnWO_4$ Single Crystals. *Appl. Phys. Lett.* **1980**, *36*, 278–279.
2. Kozma, P.; Bajgar, R. Radiation Damage of $PbWO_4$ Crystals Due to Irradiation by ^{60}Co γ-rays. *Radiat. Phys. Chem.* **2002**, *65*, 127–130.
3. Van Uitert, L. G.; Preziosi, S. Zinc Tungstates for Mirowave Maser Applications. *J. Appl. Phys.* **1962**, *33*, 2908–2909.
4. Rushbrooke, J. G.; Ansorge, R. E. Optical Fiber Readout and Performance of Small Scintillating Crystals for a Fine-Grained Gamma Detector. *Nucl. Instrum. Methods Phys. Res., Sect A* **1989**, *280*, 83–90.
5. Tanaka, K.; Miyajima, T.; Shirai, N.; Zhuang, Q.; Nakata, R. Laser Photochemical Ablation of $CdWO_4$ Studied with the Time-of-Flight Mass-Spectrometric Technique. *J. Appl. Phys.* **1995**, *77*, 6581–6587.
6. Qu, W. M.; Wlodarski, W.; Meyer, J.-U. Comparative Study on Micromorphology and Humidity Sensitive Properties of Thin-Film and Thick-Film Humidity Sensors Based on Semiconducting $MnWO_4$. *Sens. Actuators, B* **2000**, *64*, 76–82.
7. Ehrenberg, H.; Weitzel, H.; Heid, C.; Fuess, H.; Wltschek, G.; Kroener, T.; vanTol, J.; Bonnet, M. Magnetic Phase Diagrams of $MnWO_4$. *J. Phys.: Condens. Matter* **1997**, *9*, 3189–3203.
8. Driscoll, S.; Ozkan, U. S. Effect of O_2 Concentration in Selective and Complete Oxidation of 1,3-Butadiene, Furan, and Maleic Anhydride over $MnMoO_4/MoO_3$ Catalysts. *Stud. Surf. Sci. Catal.* **1994**, *82*, 367–375.
9. Cui, X. J.; Yu, S. H.; Li, L. L.; Liu, B.; Li, H. B.; Mo, M. S.; Liu, X. M. Selective Synthesis and Characterization of Single-Crystal Silver Molybdate/Tungstate Nanowires by a Hydrothermal Process. *Chem.—Eur. J.* **2004**, *10*, 218–223.
10. Liao, H. W.; Wang, Y. F.; Liu, X. M.; Li, Y. D.; Qian, Y. T. Hydrothermal Preparation and Characterization of Luminescent $CdWO_4$ Nanorods. *Chem. Mater.* **2000**, *12*, 2819–2821.
11. Yu, S. H.; Antonietti, M.; Cölfen, H.; Giersig, M. Synthesis of Very Thin 1D and 2D $CdWO_4$ Nanoparticles with Improved Fluorescence Behavior by Polymer-Controlled Crystallization. *Angew. Chem., Int. Ed.* **2002**, *41*, 2356–2360.
12. Cheng, L.; Shao, Q.; Shao, M. W.; Wei, X. W.; Wu, Z. C. Photoswitches of One-Dimensional Ag_2MO_4 (M = Cr, Mo, and W). *J. Phys. Chem. C* **2009**, *113*, 1764–1768.
13. Lasocha, W.; Lasocha, A.; Hodorowicz, S. A. Preparation and Characterization of Silver Trimolybdate. *Cryst. Res. Technol.* **1985**, *20*, 713–718.
14. Arof, A. K.; Seman, K. C.; Hashim, A. N.; Yahya, R.; Maah, M. J.; Radhakrishna, S. A New Silver Ion Conductor for Battery Applications. *Mater. Sci. Eng., B* **1995**, *31*, 249–254.
15. Bhattacharya, S.; Ghosh, A. Electrical Properties of Ion Conducting Molybdate Glasses. *J. Appl. Phys.* **2006**, *100*, 114119–114123.
16. Bhattacharya, S.; Ghosh, A. Silver Molybdate Nanoparticles, Nanowires, and Nanorods Embedded in Glass Nanocomposites. *Phys. Rev. B* **2007**, *75*, 092103–092106.
17. Hariharan, K.; Sangamithra, C. Mixed Mobile Ion Effect in Copper and Silver Molybdate Glasses. *Mater. Chem. Phys.* **1992**, *32*, 240–243.
18. Sunu, S. S.; Jayaraman, V.; Prabhu, E.; Gnanasekar, K. I.; Gnanasekaran, T. $Ag_6Mo_{10}O_{33}$—A New Silver Ion Conducting Ammonia Sensor Material. *Ionics* **2004**, *10*, 244–253.
19. Prabhu, E.; Muthuraja, S.; Gnanasekar, K. I.; Jayaraman, V.; Sivabalan, S.; Gnanasekaran, T. Ammonia Sensing Properties of Thick and Thin Films of $Ag_6Mo_{10}O_{33}$ and $Cr_{1.8}Ti_{0.2}O_{3+\delta}$. *Surf. Eng.* **2008**, *24*, 170–175.
20. Wenda, E. High Temperature Reactions in the MoO_3−Ag_2O System. *J. Therm. Anal. Calorim.* **1998**, *53*, 861–870.
21. Bréchignac, C.; Cahuzac, P.; Kebaili, N.; Lando, A.; Masson, A.; Schmidt, M. Synthesis of Silver Molybdate Clusters Driven by Laser-Annealing. *J. Chem. Phys.* **2004**, *121*, 9617–9622.

22. Nagaraju, G.; Chandrappa, G. T.; Livage, J. Synthesis and Characterization of Silver Molybdate Nanowires, Nanorods and Multipods. *Bull. Mater. Sci.* **2008**, *31*, 367–371.
23. Zhu, M. S.; Chen, P. L.; Liu, M. H. Graphene Oxide Enwrapped Ag/AgX (X = Br, Cl) Nanocomposite as a Highly Efficient Visible-Light Plasmonic Photocatalyst. *ACS Nano* **2011**, *5*, 4529–4536.
24. Zheng, Z. K.; Huang, B. B.; Qin, X. Y.; Zhang, X. Y.; Dai, Y.; Whangbo, M. H. Facile *In Situ* Synthesis of Visible-Light Plasmonic Photocatalysts M@TiO_2 (M = Au, Pt, Ag) and Evaluation of Their Photocatalytic Oxidation of Benzene to Phenol. *J. Mater. Chem.* **2011**, *21*, 9079–9087.
25. Wang, P.; Huang, B. B.; Zhang, X. Y.; Qin, X. Y.; Jin, H.; Dai, Y.; Wang, Z. Y.; Wei, J. Y.; Zhan, J.; Wang, S. Y.; Wang, J. P.; Whangbo, M. H. Highly Efficient Visible-Light Plasmonic Photocatalyst Ag@AgBr. *Chem.—Eur. J.* **2009**, *15*, 1821–1824.
26. Zhang, H.; Wang, G.; Chen, D.; Lv, X. J.; Li, J. H. Tuning Photoelectrochemical Performances of Ag−TiO_2 Nanocomposites *via* Reduction/Oxidation of Ag. *Chem. Mater.* **2008**, *20*, 6543–6549.
27. Wang, P.; Huang, B. B.; Qin, X. Y.; Zhang, X. Y.; Dai, Y.; Wei, J. Y.; Whangbo, M. H. Ag@AgCl: A Highly Efficient and Stable Photocatalyst Active under Visible Light. *Angew. Chem., Int. Ed.* **2008**, *47*, 7931–7933.
28. Yu, J. G.; Dai, G. P.; Huang, B. B. Fabrication and Characterization of Visible-Light-Driven Plasmonic Photocatalyst Ag/AgCl/TiO_2 TiO_2 Nanotube Arrays. *J. Phys. Chem. C* **2009**, *113*, 16394–16401.
29. Li, J. X.; Xu, J. H.; Dai, W. L.; Fan, K. N. Dependence of Ag Deposition Methods on the Photocatalytic Activity and Surface State of TiO_2 with Twistlike Helix Structure. *J. Phys. Chem. C* **2009**, *113*, 8343–8349.
30. Tian, Y.; Tatsuma, T. Plasmon-Induced Photoelectrochemistry at Metal Nanoparticles Supported on Nanoporous TiO_2. *Chem. Commun.* **2004**, 1810–1811.
31. Liu, Z. Y.; Sun, D. D. L.; Guo, P.; Leckie, J. O. An Efficient Bicomponent TiO_2/SnO_2 Nanofiber Photocatalyst Fabricated by Electrospinning with a Side-by-Side Dual Spinneret Method. *Nano Lett.* **2007**, *7*, 1081–1085.
32. Cao, Y.; Zhang, X. T.; Yang, W. S.; Du, H.; Bai, Y. B.; Li, T. J.; Yao, J. N. A Bicomponent TiO_2/SnO_2 Particulate Film for Photocatalysis. *Chem. Mater.* **2000**, *12*, 3445–3448.
33. Wang, P.; Huang, B. B.; Zhang, X. Y.; Qin, X. Y.; Dai, Y.; Jin, H.; Wei, J. Y.; Whangbo, M. H. Composite Semiconductor $H_2WO_4 \cdot H_2O$/AgCl as an Efficient and Stable Photocatalyst under Visible Light. *Chem.—Eur. J.* **2008**, *14*, 10543–10546.
34. Wang, Z. Y.; Huang, B. B.; Dai, Y.; Qin, X. Y.; Zhang, X. Y.; Wang, P.; Liu, H. X.; Yu, J. X. Highly Photocatalytic ZnO/In_2O_3 Heteronanostructures Synthesized by a Coprecipitation Method. *J. Phys. Chem. C* **2009**, *113*, 4612–4617.
35. Chai, S. Y.; Kim, Y. J.; Jung, M. H.; Chakraborty, A. K.; Jung, D.; Lee, W. I. Heterojunctioned BiOCl/Bi_2O_3, A New Visible Light Photocatalyst. *J. Catal.* **2009**, *262*, 144–149.
36. Cheng, H. F.; Huang, B. B.; Dai, Y.; Qin, X. Y.; Zhang, X. Y. One-Step Synthesis of the Nanostructured AgI/BiOI Composites with Highly Enhanced Visible-Light Photocatalytic Performances. *Langmuir* **2010**, *26*, 6618–6624.
37. Dong, R. X.; Chou, C. C.; Lin, J. J. Synthesis of Immobilized Silver Nanoparticles on Ionic Silicate Clay and Observed Low-Temperature Melting. *J. Mater. Chem.* **2009**, *19*, 2184–2188.
38. Jiang, H.; Moon, K.-S.; Hua, F.; Wong, C. P. Synthesis and Thermal and Wetting Properties of Tin/Silver Alloy Nanoparticles for Low Melting Point Lead-Free Solders. *Chem. Mater.* **2007**, *19*, 4482–4485.
39. Yang, N. J.; Aoki, K.; Nagasawa, H. Thermal Metallization of Silver Stearate-Coated Nanoparticles Owing to the Destruction of the Shell Structure. *J. Phys. Chem. B* **2004**, *108*, 15027–15032.
40. Yeshchenko, O. A.; Dmitruk, I. M.; Alexeenko, A. A.; Kotko, A. V. Surface Plasmon as a Probe for Melting of Silver Nanoparticles. *Nanotechnology* **2010**, *21*, 045203–1−045203−7.
41. Hu, C.; Peng, T. W.; Hu, X. X.; Nie, Y. L.; Zhou, X. F.; Qu, J. H.; He, H. Plasmon-Induced Photodegradation of Toxic Pollutants with Ag-AgI/Al_2O_3 under Visible-Light Irradiation. *J. Am. Chem. Soc.* **2010**, *132*, 857–862.
42. Tamai, T.; Watanabe, M.; Teramura, T.; Nishioka, N.; Matsukawa, K. Metal Nanoparticle/Polymer Hybrid Particles: The Catalytic Activity of Metal Nanoparticles Formed on the Surface of Polymer Particles by UV-Irradiation. *Macromol. Symp.* **2009**, *282*, 199–204.
43. Shao, M. W.; Lu, L.; Wang, H.; Wang, S.; Zhang, M. L.; Ma, D. D. D.; Lee, S. T. An Ultrasensitive Method: Surface-Enhanced Raman Scattering of Ag Nanoparticles from β-Silver Vanadate and Copper. *Chem. Commun.* **2008**, 2310–2312.
44. Saison, T.; Chemin, N.; Chaneac, C.; Durupthy, O.; Ruaux, V.; Mariey, L.; Mauge, F.; Beaunier, P.; Jolivet, J. P. Bi_2O_3, $BiVO_4$, and Bi_2WO_6: Impact of Surface Properties on Photocatalytic Activity under Visible Light. *J. Phys. Chem. C* **2011**, *115*, 5657–5666.
45. Li, X.; Ye, J. H. Photocatalytic Degradation of Rhodamine B over $Pb_3Nb_4O_{13}$/Fumed SiO_2 Composite under Visible Light Irradiation. *J. Phys. Chem. C* **2007**, *111*, 13109–13116.
46. Fu, H. B.; Pan, C. S.; Yao, W. Q.; Zhu, Y. F. Visible-Light-Induced Degradation of Rhodamine B by Nanosized Bi_2WO_6. *J. Phys. Chem. B* **2005**, *109*, 22432–22439.
47. Watanabe, T.; Takizawa, T.; Honda, K. Photocatalysis through Excitation of Adsorbates. 1. Highly Efficient N-Deethylation of Rhodamine B Adsorbed to CdS. *J. Phys. Chem.* **1977**, *81*, 1845–1851.
48. Agostini, G.; Usseglio, S.; Groppo, E.; Uddin, M. J.; Prestipino, C.; Bordiga, S.; Zecchina, A.; Solari, P. L.; Lamberti, C. From Isolated Ag^+ Ions to Aggregated Ag^0 Nanoclusters in Silver-Exchanged Engelhard Titanosilicate (ETS-10) Molecular Sieve: Reversible Behavior. *Chem. Mater.* **2009**, *21*, 1343–1353.
49. Zeng, J. B.; Jia, H. Y.; An, J.; Han, X. X.; Xu, W. Q.; Zhao, B.; Ozaki, Y. Preparation and SERS Study of Triangular Silver Nanoparticle Self-Assembled Films. *J. Raman. Spectrosc.* **2008**, *39*, 1673–1678.
50. Zou, X. Q.; Dong, S. J. Surface-Enhanced Raman Scattering Studies on Aggregated Silver Nanoplates in Aqueous Solution. *J. Phys. Chem. B* **2006**, *110*, 21545–21550.
51. Phuruangrat, A.; Thongtem, T.; Thongtem, S. Synthesis of Lead Molybdate and Lead Tungstate *via* Microwave Irradiation Method. *J. Cryst. Growth.* **2009**, *311*, 4076–4081.
52. Yoon, J.-W.; Ryu, J. H.; Shim, K. B. Photoluminescence in Nanocrystalline $MMoO_4$ (M = Ca, Ba) Synthesized by a Polymerized Complex Method. *Mater. Sci. Eng., B* **2006**, *127*, 154–158.
53. Wang, J. M.; Gao, L. Wet Chemical Synthesis of Ultralong and Straight Single-Crystalline ZnO Nanowires and Their Excellent UV Emission Properties. *J. Mater. Chem.* **2003**, *13*, 2551–2554.
54. Al-Kady, A. S.; Gaber, M.; Hussein, M. M.; Ebeid, E.-Z. M. Fluorescence Enhancement of Coumarin Thiourea Derivatives by Hg^{2+}, Ag^+, and Silver Nanoparticles. *J. Phys. Chem. A* **2009**, *113*, 9474–9484.
55. Qu, H.; Cao, L. X.; Su, G.; Liu, W.; Sun, Y. G.; Dong, B. H. Effect of Ultraviolet Irradiation on Luminescence Properties of Undoped ZnS and ZnS:Ag Nanoparticles. *J. Appl. Phys.* **2009**, *106*, 093506-1–093506-6.
56. Dabbousi, B. O.; Rodriguez-Viejo, J.; Mikulec, F. V.; Heine, J. R.; Mattoussi, H.; Ober, R.; Jensen, K. F.; Bawendi, M. G. (CdSe)ZnS Core−Shell Quantum Dots: Synthesis and Characterization of a Size Series of Highly Luminescent Nanocrystallites. *J. Phys. Chem. B* **1997**, *101*, 9463–9475.
57. Watanabe, H.; Hayazawa, N.; Inouye, Y.; Kawata, S. DFT Vibrational Calculations of Rhodamine 6G Adsorbed on Silver: Analysis of Tip-Enhanced Raman Spectroscopy. *J. Phys. Chem. B* **2005**, *109*, 5012–5020.
58. Hildebrandt, P.; Stockburger, M. Surface-Enhanced Resonance Raman Spectroscopy of Rhodamine 6G Absorbed on Colloidal Silver. *J. Phys. Chem.* **1984**, *88*, 5935–5944.
59. Raimondo, A.; Mandanici, A.; Ramos, M. A.; Rodrigo, J. G.; Armellini, C.; Cutroni, M.; Vieira, S. Experimental Study of

the Thermal Expansion of $(AgI)_{0.67}(Ag_2MoO_4)_{0.33}$ Ionic Glass from 5 to 300 K. *Philos. Mag.* **2008**, *88*, 3973–3978.
60. Sanson, A.; Rocca, F.; Armellini, C.; Ahmed, S.; Grisenti, R. Local Study on the MoO_4 Units in AgI-Doped Silver Molybdate Glasses. *J. Non-Cryst. Solids* **2008**, *354*, 94–97.
61. Sanson, A.; Rocca, F.; Dalba, G.; Fornasini, P.; Grisenti, R. Influence of Temperature on the Local Structure around Iodine in Fast-Ion-Conducting AgI: Ag_2MoO_4 Glasses. *New J. Phys.* **2007**, *9*, 88-1–88-14.
62. Bao, S. J.; Bao, Q. L.; Li, C. M.; Chen, T. P.; Sun, C. Q.; Dong, Z. L.; Gan, Y.; Zhang, J. Synthesis and Electrical Transport of Novel Channel-Structured β-$AgVO_3$. *Small* **2007**, *3*, 1174–1177.
63. Song, J. M.; Lin, Y. Z.; Yao, H. B.; Fan, F. J.; Li, X. G.; Yu, S. H. Superlong β-$AgVO_3$ Nanoribbons: High-Yield Synthesis vby a Pyridine-Assisted Solution Approach, Their Stability, Electrical and Electrochemical Properties. *ACS Nano* **2009**, *3*, 653–660.
64. Mai, L. Q.; Lao, C. S.; Hu, B.; Zhou, J.; Qi, Y. Y.; Chen, W.; Gu, E. D.; Wang, Z. L. Synthesis and Electrical Transport of Single-Crystal $NH_4V_3O_8$ Nanobelts. *J. Phys. Chem. B* **2006**, *110*, 18138–18141.
65. Chakraborty, S.; Bera, M. K.; Dalapati, G. K.; Paramanik, D.; Varma, S.; Bose, P. K.; Bhattacharya, S.; Maiti, C. K. Leakage Current Characteristics and the Energy Band Diagram of $Al/ZrO_2/Si_{0.3}Ge_{0.7}$ Hetero-MIS Structures. *Semicond. Sci. Technol.* **2006**, *21*, 467–472.
66. Golan, G.; Axelevitch, A.; Sigalov, B.; Gorenstein, B. Investigation of Phase Transition Mechanism in Vanadium Oxide Thin Films. *J. Optoelectron. Adv. Mater.* **2004**, *6*, 189–195.